

Numerical Modeling of Powder Gas Interaction Relative to Laser Powder Bed Fusion Process

Xuxiao Li

Department of Mechanical Engineering,
University of Utah,
Utah, UT 84112
e-mail: xuxiao.li@utah.edu

Wenda Tan¹

Mem. ASME
Department of Mechanical Engineering,
University of Utah,
Utah, UT 84112
e-mail: wenda.tan@mech.utah.edu

The powder motion induced by the gas flow has been identified as one of the critical phenomena in laser powder bed fusion processes that significantly affect the build quality. However, the gas dynamics and its induced driving forces for the powder motions have not been well quantified. A numerical model is developed to investigate such powder-gas interactions. With a combination of computational fluid dynamics and particle tracking techniques, the model is capable of simulating the transient gas flow field surrounding the powder and the forces exerted on powder surfaces. The interaction between metal powders and a free jet is investigated with the current model. In the simulation results, the entrainment and the ejection motions of powders with respect to the free jet can be predicted. It is found that the driving forces of these motions are majorly contributed by the pressure differences in the gas flow surrounding the powder, and the powders can also interact with the jet to significantly alter the flow field. Quantities that are difficult to measure by experiments are quantified by the simulations, such as the velocity/pressure fields in the gas as well as the subjected forces and torques on powders. Such quantitative information provides insights about the mechanisms of the powder-gas interaction in laser powder bed fusion processes. [DOI: 10.1115/1.4048443]

Keywords: additive manufacturing, laser processes, modeling and simulation

1 Introduction

In the laser powder bed fusion (LPBF) process, a laser is directed toward and scans across a pre-deposited powder bed typically made of metal alloys. The metal powders are melted upon by the laser heating to form a molten pool and are consolidated to attribute to the built part when the laser is moved away. The building process then repeats in a layer-by-layer manner to create the desired bulk geometries. Although LPBF receives increasing applications in the manufacturing industry [1], significant uncertainties of build quality are found in LPBF parts [2–4]. One source of such uncertainties is the powder motion in LPBF processes. It has recently been revealed by high-speed optical imaging [5–7] and X-ray imaging [8–10] that the powders tend to dislocate from its original location during the laser scanning. Specifically, the powders at a distance can be entrained toward the laser-shined region, while the powders nearby can be ejected from the laser-shined region.

It has been reported that the powder motions have a significant influence on the build quality of LPBF. The ejected powders, when landing back on the build surface, can deteriorate the surface roughness [11,12], distort the molten pool geometry [13], or cause insufficient melting and lack-of-fusion defects [8]. Moreover, the apparent stochastic nature of these powder motions [5] randomizes the mass distribution of the powder bed and increases the uncertainty of the build quality.

In literature, the origin of the powder motion has been explained based on experimental observations and basic principles of physics [7,8]. The intense laser heating of the metal powders triggers metal vaporization. A metal vapor jet is formed that originates from the molten pool surface and expands into the ambient gas (typically argon). The metal vapor jet then induces an argon gas flow that entrains the surrounding powders toward the jet, and once near the jet, the powders are immediately ejected following the expanding vapor flow. Despite such a qualitative understanding of the powder-gas interaction in LPBF, the transient flow surrounding the powders as well as the gas-flow-induced forces on the powder surface have not been well quantified. Such quantitative information can be crucial to construct mappings between the powder motion to process parameters and to achieve the control of the powder motions.

Given that experimentally measuring the flow velocities and forces at such a small scale (~tens of microns) can be very difficult to achieve, the multiphysics simulation is a promising tool for obtaining this quantitative information. In literature, the multiphysics simulations have been used to study the evolution of the molten pool and quantify physical phenomena such as powder melting and merging [14], keyholing [15,16] and lack-of-fusion [17], the resultant pore formation [18,19], as well as balling [20]. For the gas flow, the steady-state flow field has been simulated [5,21], and a recent work revealed the transient development of the vapor jet [22]. But to the author's knowledge, no simulation work on the powder-gas interaction in LPBF can be found in the literature. This lack of simulation effort can be attributed to the complexity of physics in the powder-gas interaction. Indeed, three phases, solid (metal powder and substrate), liquid (molten pool), and gas (metal vapor and argon) have to be modeled simultaneously and consistently to fully resolve the powder-gas interaction in LPBF.

In this work, a numerical model is developed to investigate the powder-gas interaction in LPBF. An incremental approach is taken to cope with the complexity of physics. In the current model, significant thermal effects (e.g., powder melting and vaporization) are neglected. The solid and gaseous phases are resolved, while the liquid phase is neglected. The current model will provide the foundation for a more comprehensive model where all three phases and thermal effects are incorporated. The simulation results demonstrate the capability of the current model to capture the general trends of powder motions in LPBF and to quantify the transient gas flow field and the forces on the powders.

2 Model Description

A two-dimensional (2D) model is developed to capture the gas dynamics and the gas-flow-induced powder motions in an LPBF process. A computational fluid dynamics (CFD) module is used to calculate the pressure, velocity, and temperature field in the gaseous phase. A particle-tracking (PT) module is used to calculate the forces, velocities, and positions of powders. The CFD and PT modules need to be coordinated to ensure consistent computations.

2.1 Computational Fluid Dynamics Module. In the gaseous phase, the conservation equations of mass, momentum, and energy for compressible flow constitute the governing equations to be solved, as written in Eqs. (1)–(3). The gas is assumed to be ideal and the ideal gas law provides the thermodynamic relation to

¹Corresponding author.

Manuscript received April 4, 2020; final manuscript received June 6, 2020; published online November 11, 2020. Assoc. Editor: Steven Schmid.

close Eqs. (1)–(3).

$$\frac{\partial \rho}{\partial t} + \nabla \cdot (\rho \vec{V}) = 0 \quad (1)$$

$$\frac{\partial}{\partial t} (\rho \vec{V}) + \nabla \cdot (\rho \vec{V} \vec{V}) = -\nabla p + \nabla \cdot \tau \quad (2)$$

$$\begin{aligned} \frac{\partial}{\partial t} (\rho e) + \nabla \cdot (\rho e \vec{V}) = \nabla \cdot (p \vec{V}) \\ + \nabla \cdot (\tau \vec{V}) + \nabla \cdot (k \nabla T) \end{aligned} \quad (3)$$

In Eqs. (1)–(3), ρ is the density, \vec{V} is the velocity, p is the pressure, τ is the viscous tensor, \vec{g} is the gravitational acceleration, e is the total energy (internal energy and kinetic energy), k is the thermal conductivity, and T is the temperature. An in-house finite-volume CFD solver [23] is used to discretized and solve the governing equations for the gaseous phase.

2.2 Particle-Tracking Module. Newton's equations of motion are solved to track the velocities of each individual powder, as written in Eqs. (4) and (5).

$$m_p \frac{d\vec{V}_{pc}}{dt} = \oint_{\partial S} \vec{F}_f dS + m_p \vec{g} + \vec{F}_{col} \quad (4)$$

$$I_p \frac{d\vec{\omega}}{dt} = \oint_{\partial S} \vec{r} \times \vec{F}_f dS \quad (5)$$

Equation (4) solves the translational velocity of powders where m_p is the powder mass and \vec{V}_{pc} is the velocity of the powder center. On the right-hand-side (RHS), the first term is the integration of the fluid-induced force (\vec{F}_f) on the powder surface (∂S), the second term is the gravitational force, and the third term is the force due to powder-powder or powder-wall collisions. Here, the collision force \vec{F}_{col} is simplified to be a short-range repulsion force [24] which is detailed later. Equation (5) solves the rotational velocity of powders where I_p is the moment of inertia of powder and $\vec{\omega}$ is the angular velocity of powder. The RHS is the integration of the fluid-induced torque on the powder surface. The positions of each powder, including the positions of powder center (x_{pc}, y_{pc}) and the angular position θ , are updated according to the powder velocities ($\vec{V}_{pc}, \vec{\omega}$) by the Gear's time integration scheme [25].

The collision force on the i th particle due to its collision with the j th particle can be calculated by

$$\vec{F}_{ij} = \frac{m_i g}{\varepsilon} \left(\max \left(\frac{R_i + R_j + \delta - d_{ij}}{\delta}, 0 \right) \right)^2 \vec{n}_{ij} \quad (6)$$

In Eq. (6), $m_i g$ is the gravitational force of the i th particle, R_i and R_j are the radii of the i th and j th particle, d_{ij} is the distance between the centers of the i th and j th particle, and \vec{n}_{ij} is a unit vector pointing from the i th particle's center to the j th particle's center. The ε and δ are two collision parameters where ε controls the "stiffness" and δ controls the "range" of the collision force [24]. In all the simulations, the choice of $\varepsilon = 5 \times 10^{-5}$ and $\delta = 0.5h$ (h being the smallest mesh size in the domain) is applied based on the guidelines given in Ref. [24].

2.3 Coordination of Modules. The coordination between the CFD and PT module is demonstrated in Fig. 1. The CFD module calculation is carried out on a Cartesian grid where powders (e.g., the large circle) tracked by the PT module are overlaid. The grid cells whose centroid lies within the powder is identified as solid cells (shaded cells) while the cells whose centroid lies outside the powder are identified as the gas cells. The simulation advances in

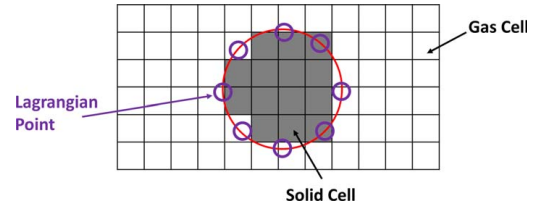


Fig. 1 Coordination between the CFD and the PT module

time as the CFD module updates the pressure and velocity in each gas cell, and the PT module updates the velocities ($\vec{V}_{pc}, \vec{\omega}$) for each powder.

The interaction between the two modules is as follows. The location and speed of each particle is first identified by the PT module and passed to the CFD module. The pressure and velocity in the solid cells will be specified as the boundary conditions for the CFD module. Specifically, the pressure in the solid cells is extrapolated from the gas. The velocity in the solid cells is assigned as the local powder velocity obtained from the PT module, and a no-slip condition is assigned at the solid–gas interface [26]. The CFD module provides the fluid-induced force (\vec{F}_f in Eqs. (4) and (5)) to the PT module. Specifically, the Lagrangian points [27] are defined on the surface of each powder (see Fig. 1) and are fixed relative to the powder frame. The pressure and viscous stress are evaluated at each cell centroid of the Cartesian grid from CFD calculations and are used to interpolate the fluid-induced forces (\vec{F}_f) for each Lagrangian point. The surface integrals in Eqs. (4) and (5) are then obtained by integrating the force and torque over all Lagrangian points on the powder surface.

For each discrete time-step of the simulation, the pressure and velocity in each Cartesian cell (both solid and gas) as well as the velocities and positions of each powder are determined. These quantities are then updated for the next time-step with the procedure summarized as the following steps:

- (1) Interpolate the fluid-induced forces on Lagrangian points.
- (2) Evaluate the RHS of Eqs. (4)–(5), and update powder velocities and positions with the PT module.
- (3) Based on the updated powder positions, identify solid and gas cells.
- (4) Assign the pressure and velocity in solid cells, with the pressure in gas cells and the updated powder velocities.
- (5) Update the pressure and velocity in gas cells by solving Eqs. (1)–(3) with the CFD module.

3 Problem Definition

Due to the complexity of physics in a real LPBF process, a simplified problem is formulated to resemble the process of LPBF but with simplified physics. The configuration of the problem is shown in Fig. 2. The liquid phase (molten metal) is neglected, and an artificial

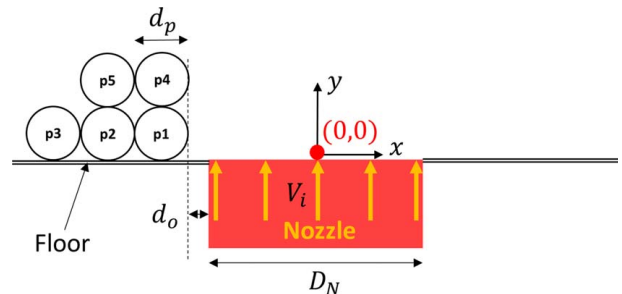


Fig. 2 Configuration of the simplified problem (powder-jet interaction problem)

nozzle is defined to stimulate a free jet that resembles the metal vapor jet initiated from the molten pool in a real LPBF process. The nozzle has a diameter D_N and a uniform inlet velocity of V_i . A set of powder particles is initially positioned at an offset distance d_o from the nozzle and is placed on a solid floor. The powder particles have a uniform diameter of d_p and are regularly positioned, such as p1–p5 shown in Fig. 2. It is noted that in some LPBF processes, a cross-flow is applied above the powder bed to blow away the spattered powders/droplets that are ejected by the vapor jet [28,29]. Such effects are not captured in the simplified setup of Fig. 2. In the current work, only the powder-jet interaction is resolved, and the cross-flow effects are considered as part of future works.

In this work, the simplification is made that any significant change of temperature will not be considered. The laser heating, powder melting, and vaporization, as well as the powder merging with the molten pool, are not modeled. Moreover, the inlet temperature of the nozzle is kept at room temperature. With the major thermal effects ignored, the current work is focused on the dynamics of the interaction between the powder(s) and a nearly isothermal jet. This simplified powder-jet interaction model is the first step to reveal the complex mechanisms of powder-gas interaction in a real LPBF process. A detailed discussion on the implications of the current simplifications will be given in the later text.

The design of the calculation domain is illustrated in Fig. 3. The entire domain is a rectangle box (the outer contour) that is symmetric with respect to the Y -axis. A Cartesian mesh is applied for the entire domain, and the mesh is refined in the region where the powder-jet interaction occurs (the inner box). The inlet boundary condition is applied at the $Y=0$ plane where the nozzle is located, while the rest of the $Y=0$ plane is applied with the wall boundary condition. All the other boundaries are applied with the outlet boundary condition. It is noted that the calculation domain is large enough such that the boundary conditions in the far-field do not significantly affect the powder-jet interaction in the fine mesh region.

4 Results and Discussion

The parameters of the powder-jet interaction (D_N , V_i , d_o , d_p) are defined such that the configuration can resemble a typical LPBF process. Based on the typical experimental observations [6,9], the following values are chosen: $D_N=200\ \mu\text{m}$, $V_i=500\ \text{m/s}$, $d_o=10\ \mu\text{m}$, and $d_p=50\ \mu\text{m}$. The powder material is chosen to be Ti-6Al-4V, and the gas material is chosen to be argon. The density of argon gas obeys the ideal gas law. The density of powder and the viscosity of argon gas are assumed to be temperature independent, as the temperature variation in the simulations is not significant. These material properties are listed in Table 1.

A series of case studies (listed in Table 2) is designed to investigate the formulated problem. In order to anatomize the details of powder-jet interaction, the cases are studied in which only a single powder particle is positioned beside the nozzle. Three

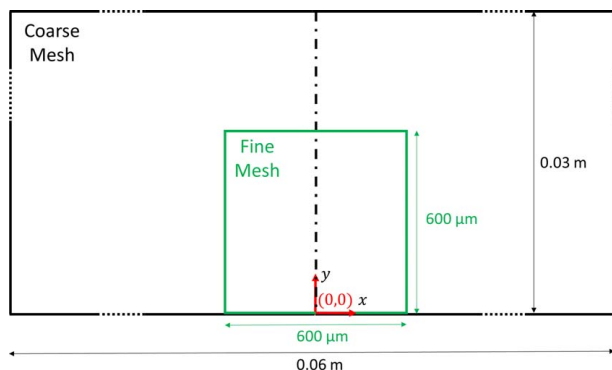


Fig. 3 The design of the calculation domain

Table 1 Material properties of Ti-6Al-4V and argon gas used for simulation

Material property	Ti-6Al-4V [30]	Argon [31]	Unit
Density	4420 ^a	1.78 ^b	kg m ⁻³
Viscosity		2.16×10^{-5a}	Pa s

^aAssumed to be temperature independent. Values at 300 K are used.

^bFollows the ideal gas law. The given value is at 300 K.

different initial positions of the powder particle are investigated (Case 1–3), which correspond to the locations of p1, p2, and p3 in Fig. 2. After the single-particle cases, a more realistic case is investigated in which four powder particles (corresponding to locations of p1, p2, p4, and p5 in Fig. 2) are initially positioned beside the jet. In all the simulations, a uniform mesh size of $5\ \mu\text{m}$ is applied in the fine mesh region to resolve the particle diameter ($50\ \mu\text{m}$). The time-step size is set to be $0.01\ \mu\text{s}$. The time-step size is chosen to be small enough such that the maximum Courant number is less than one. The simulation is carried out until all the major events of powder-jet interaction are completed; a total simulation time of $500\ \mu\text{s}$ is selected for all simulations.

4.1 Interaction Between Jet and One Single Particle. The simulation result for Case 2 is first discussed as a typical case for the single-particle studies. The simulated gauge pressure (the difference between absolute pressure and 1 atm) and velocity field at four key time frames are shown in Fig. 4(a). The displacements (d_x , d_y), velocities (V_x , V_y), the subjected forces (F_x , F_y), angular position θ , angular velocity ω , and the subjected torque τ of the powder particle with respect to time are recorded and shown in Fig. 4(b). The video of the simulation is given in Video S1 available in the Supplemental Materials on the ASME Digital Collection.

Right after the simulation starts, the jet initiates from the nozzle and rapidly expands into the ambient gas. It is shown in Fig. 4(a) that, at $2.5\ \mu\text{s}$, the jet expansion creates a large vortex that drives the powder particle upwards and toward the jet as indicated by the streamlines surrounding the particle. This initial vortex rapidly propagates upwards and away from the particle with the free expansion of the jet at a velocity $\sim 500\ \text{m/s}$, and it only has a significant influence on the powder motion for a very short period of time. It is observed in Fig. 4(b) that the initial vortex leads to an “impulse” of the powder forces F_x and F_y at the beginning of the simulation, which corresponds to a sharp increase of the powder velocities (V_x increases to $\sim 0.25\ \text{m/s}$ and V_y increases to $\sim 0.2\ \text{m/s}$). Thereafter, the powder forces are reduced to small values as the initial vortex propagates away from the powder.

During the time period of $\sim 10\ \mu\text{s}$ – $150\ \mu\text{s}$, the powder particle gradually accelerates along the $+X$ -direction and decelerates along the $+Y$ -direction, as shown in Fig. 4(b). The “entrainment” of the particle toward the jet (along $+X$ -direction) has an acceleration $\sim 3500\ \text{m/s}^2$ and a typical velocity $\sim 0.5\ \text{m/s}$. The entrainment motion can be explained by examining the streamlines at a typical time frame during this time period, as shown at $75\ \mu\text{s}$ in

Table 2 Powder-jet interaction study

	Case no.	Corresponding particle(s) in Fig. 2	Initial coordinates of particle center (μm)
Single particle	1	p1	(−135, 25)
	2	p2	(−185, 25)
	3	p3	(−215, 25)
Multiple particles	4	p1, p2, p4, p5	(−135, 25); (−185, 25); (−135, 75); (−185, 75)

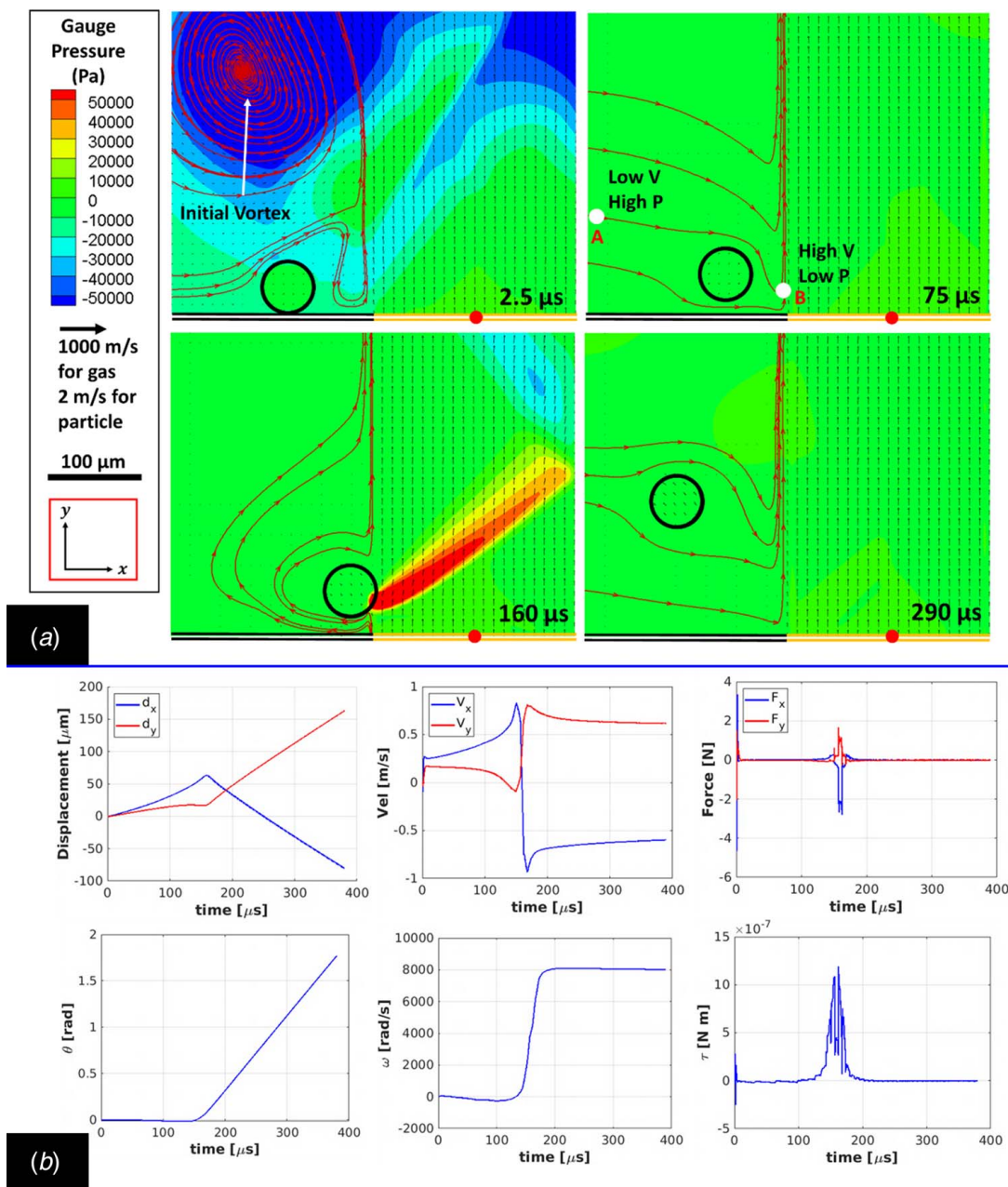


Fig. 4 (a) The pressure and velocity field at 2.5 μs , 75 μs , 160 μs , and 290 μs of the simulation for the powder-jet interaction of a single powder particle (Case 2 in Table 2). The contours show the gauge pressure and the arrows show the velocity field. The length of the arrow key represents 1000 m/s if the velocity arrow is in the gas and 2 m/s if in the velocity arrow is in the particle. The double line indicates the location of the floor and the nozzle. The small dot on the double line is the origin of the coordinate system. The solid lines with arrows show the streamlines surrounding the powder particle. (b) The displacements, velocities, the subjected forces, angular position θ , angular velocity ω , and the subjected torque τ of the powder particle with respect time for the single-particle simulation in (a).

Fig. 4(a). Two points, A and B, along a typical streamline are highlighted for the analysis. Point A is away from the jet and has a small velocity (~ 5 m/s) along the streamline. According to the Bernoulli principle, point A is associated with a larger gauge pressure (~ -300 Pa). Point B is located near the inlet of the jet and has a large streamline-wise velocity (~ 50 m/s). Accordingly, point B has a lower gauge pressure (~ -2000 Pa) compared to point A. Due to the pressure difference between points A and B, the entrained gas bends toward the corner of the free jet (point B) and is then directed upwards along the expansion of the jet. Following this flow pattern, the particle is entrained and accelerates toward the corner of the jet.

As the powder particle continues to be entrained toward the jet, it eventually touches upon the jet around 160 μs (Fig. 4(a)). A significant change of streamline pattern occurs as the lower-right corner of the particle blocks the gas flow. The blocking powder forces the gas flow velocity to decelerate to the powder's velocity at the powder surface due to the no-slip condition at the gas-powder interface. The powder's velocity (~ 1 m/s) is far less than the jet inlet velocity (500 m/s). Therefore, the gas flow velocity is dramatically decreased from the inlet to the region near the powder surface. As a result, a focused high-pressure region ($\sim 40,000$ Pa) is formed at the lower-right corner of the particle. This high pressure then "kicks" the particle along $-X$ and $+Y$ -direction, as indicated by the

“impulse” of powder forces in Fig. 4(b) ($F_x \sim -2$ N and $F_y \sim 2$ N) and the sharp change of the powder velocities (V_x changes from ~ 0.8 m/s to ~ -0.9 m/s and V_y changes from ~ -0.1 m/s to ~ 0.8 m/s); the acceleration of this dramatic transition is $\sim 80,000$ m/s². Also, there is an impulse of the torque τ around $160 \mu\text{s}$, and accordingly, the angular velocity ω of the powder sharply increases to ~ 8000 rad/s. This torque is attributed to the tangential viscous force on the powder surface created by the velocity difference between the vapor and the powder particle on the right side of the particle surface.

Resulted from the “kick,” the powder particle is ejected away from the jet and continues to move along the $-X$ and $+Y$ -direction at a typical velocity ~ 1 m/s, as shown by the velocity plot in Fig. 4(b). It is noted that the ejection of the particle is against the surrounding flow, as the latter tends to entrain the particle toward the jet (the streamlines at $290 \mu\text{s}$ in Fig. 4(a)). Finally, the particle is out of the calculation domain $\sim 390 \mu\text{s}$, after which the particle is not tracked anymore in Fig. 4(b).

Consistent results can be obtained when the initial position of the powder particle is varied. Figure 5 shows the V_x and ω with respect to time for Case 1–3 (Table 2). The videos for Case 1 and 3 are given in Videos S2 and S3. It is observed that all three simulations produce a similar trend for the evolution of V_x and ω . It is noted that for p1, the powder particle has a relatively short time period for the entrainment before it is ejected away from the jet, which is due to the proximity of the particle to the jet initially.

The single-particle simulations have revealed the powder-jet interaction in which the powder is driven by the surrounding gas flow to have the entrainment and ejection motions, while the gas flow can also be altered significantly by the powder blocking the jet. The simulated entrainment and ejection motions are analogous to those observed in LPBF processes. As a general comparison, the magnitude of powder entrainment and ejection velocity observed in LPBF processes is around 1 m/s and 5 m/s [6,8,9], while those from the current simulations are about 0.5 m/s and 1 m/s. The powder motions predicted by the current model can reasonably match the trends observed in experiments. However, the powder velocity is observed to be larger than the model prediction. This is possible because the major thermal effects have been ignored in the model. Specifically, the maximum temperature of the vapor jet can be around the boiling temperature (~ 3000 K), which is much higher than the assumed inlet temperature (room temperature, 300 K). The high temperature in the experiment tends to increase the viscosity in the gaseous phase, which can significantly increase the fluid-induced force on powders and hence the powder velocity [6]. Even with this discrepancy, the simulations still provide insightful information regarding the powder-jet interaction, such as pressure and velocity field, forces and torque on the powder, etc., which are difficult to measure by experiments.

4.2 Interaction Between Jet and Multiple Particles. The interaction between the jet and four powder particles is investigated as a more realistic case in which the powder collisions as well as the powder-jet interaction are considered (Case 4 in Table 2). A time sequence of the simulated gauge pressure and velocity field is given in Figs. 6(a)–6(f). The corresponding video is given in Video S4. Particle 1 is the first powder particle to be entrained and come in contact with the jet (Fig. 6(a)), as it is the closest particle to the low-pressure region at the left corner of the jet (point B in Fig. 4(b)). Thereafter, particle 1 is ejected from the jet and sequentially collides with Particles 2 and 3 (Figs. 6(b) and 6(c)). Resulted from the collisions, particle 1 has a significant reduction in its momentum (both in the X - and Y -direction), particle 3 is directed toward the jet and is subsequently ejected (Figs. 6(c) and 6(d)), and particle 2 gains a negative X velocity and moves away from the jet (Fig. 6(d)). Then, particle 1 is slowly entrained toward the jet (Fig. 6(e)) until it comes in contact with the jet for the second time and is subsequently ejected (Fig. 6(f)). It is noted that at the last time frame of the sequence (Fig. 6(f)), particles 2 and 3 have moved out of the calculation domain. This result demonstrates that, despite the simplified collision model, the general trend of powder collisions can be captured for the powder-jet interaction under investigation.

5 Summary and Future Work

In this work, a numerical model is established to investigate the powder-gas interaction in LPBF processes. The powder-gas interaction in a real LPBF process is simplified where the powder melting and metal vaporization is neglected, and an artificial free jet is used to model the metal vapor jet. In the study of the powder-jet interaction, the simulation results have shown the trend of powders being entrained toward and subsequently ejected from the jet. It is also found that powders can cut into the jet to alter its surrounding flow field significantly. The simulated powder velocity for the entrainment (~ 0.5 m/s) and ejection (~ 1 m/s) motion can reasonably match with experimentally observed entrainment (~ 1 m/s) and ejection (~ 5 m/s) velocity in literature. The simulations provide insights into the driving forces for the powder motions by quantifying the pressure and velocity field, etc., which are difficult to measure by experiments. The driving forces can be attributed to the pressure differences in the gas flow surrounding the powder, as summarized below:

- When the powder is away from the jet, the gas velocity is increased from near the powder (~ 5 m/s) to the region near the jet (~ 50 m/s). By the Bernoulli principle, the pressure is decreased from the near the powder toward the jet with a pressure difference ~ 2000 Pa, which gradually entrains the powder toward the jet at an acceleration of ~ 3500 m/s² and a typical velocity of ~ 0.5 m/s.

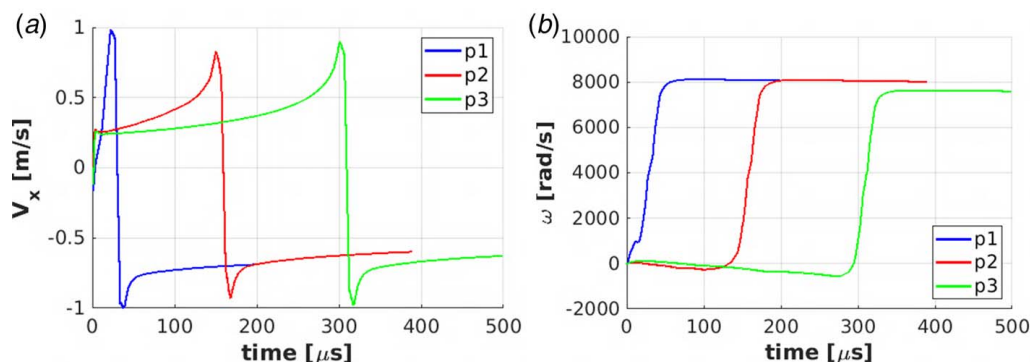


Fig. 5 The X-velocity (a) and angular velocity (b) with respect to time for the powder-jet interaction of a single powder with different initial positions (Case 1–3 in Table 2). For each simulation, the powder is tracked until it has moved out of the calculation domain.

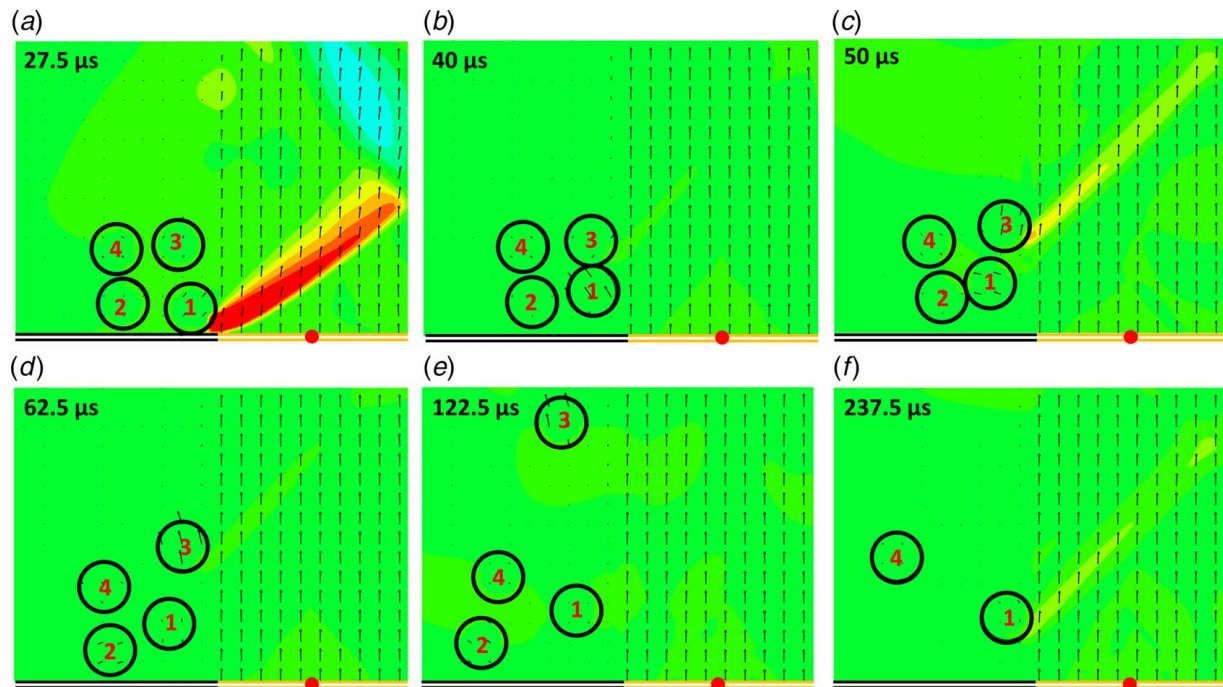


Fig. 6 The time sequence of the simulated pressure and velocity field for the powder-jet interaction with multiple powders (Case 4 in Table 2). The contours show the gauge pressure and the arrows show the velocity field. The double line indicates the locations of the floor and the nozzle. The small dot on the double line is the origin of the coordinate system.

- When the powder comes into contact with the jet, the gas velocity dramatically decreases from the jet inlet (~ 500 m/s) to almost zero at the powder surface in contact with the jet. Therefore, a high-pressure region ($\sim 40,000$ Pa) is formed where the powder blocks the jet and abruptly ejects the powder away from the jet at an acceleration of $\sim 80,000$ m/s² and a typical velocity of ~ 1 m/s.

Since this is the first step to model the very complicated powder-gas interaction in the LPBF process, the simplification is made that significant thermal effects are neglected. Specifically, the laser heating and the phase change (melting and vaporization) of the powder are not considered. The inlet temperature of the jet is kept at room temperature. The implications of these simplifications are discussed as follows:

- In real LPBF, powders that are directly illuminated by the laser are typically melted to form the molten pool. Once the molten pool is formed, the entrained powders can be subsumed into the molten pool without being ejected by the vapor jet [6,7,9]. This type of powder motion cannot be captured in the simplified powder-jet setup.
- In real LPBF, intensive heating of the powder (by laser or the vapor jet) may even cause vaporization on the powder surface. This can lead to another type of powder-gas interaction: the metal vapor exerting recoil pressure on the powder surface [6,7]. This type of powder-gas interaction cannot be captured in the current model.
- The vapor jet initiated from the molten pool surface can have a significantly different flow profile than the simplified jet applied in the current setup. In real LPBF, the “inlet” velocity profile of the vapor jet may not be a uniform profile and can be dynamically changing with the unstable molten pool [10]. This can lead to different velocity directions and magnitude for the powder ejection. Moreover, the high temperature in the gas flow and its effects on the material properties and powder-gas interaction are not considered in the current model, which may introduce errors into the predictions of powder motion.

Although the simplifications compromise the physical fidelity of the model, the current work demonstrates the model’s capability to capture the general trends of the powder-gas interaction relative to the LPBF process. Moreover, it provides the foundation for a series of future works, including the modeling of laser heating, phase change of powders (melting and vaporization), keyhole formation, and molten pool fluid flow. It is believed that the physical fidelity can be largely improved once these additional physics are incorporated into the current model.

Acknowledgment

The authors wish to gratefully acknowledge the technical support from the Center for High-Performance Computing at the University of Utah.

Funding Data

- This work is financially supported by the National Science Foundation under Grant No. CMMI-1933368.

Conflict of Interest

There are no conflicts of interest.

Data Availability Statement

The datasets generated and supporting the findings of this article are obtainable from the corresponding author upon reasonable request. The authors attest that all data for this study are included in the paper.

References

- [1] Huang, Y., Leu, M. C., Mazumder, J., and Donmez, A., 2015, “Additive Manufacturing: Current State, Future Potential, Gaps and Needs, and Recommendations,” *ASME J. Manuf. Sci. Eng.*, **137**(1), p. 014001.

- [2] Mahmoudi, M., Ezzat, A. A., and Elwany, A., 2019, "Layerwise Anomaly Detection in Laser Powder-Bed Fusion Metal Additive Manufacturing," *ASME J. Manuf. Sci. Eng.*, **141**(3), p. 031002.
- [3] Imani, F., Gaikwad, A., Montazeri, M., Rao, P., Yang, H., and Reutzel, E., 2018, "Process Mapping and in-Process Monitoring of Porosity in Laser Powder Bed Fusion Using Layerwise Optical Imaging," *ASME J. Manuf. Sci. Eng.*, **140**(10), p. 101009.
- [4] Shrestha, S., Starr, T., and Chou, K., 2019, "A Study of Keyhole Porosity in Selective Laser Melting: Single-Track Scanning With Micro-CT Analysis," *ASME J. Manuf. Sci. Eng.*, **141**(7), pp. 1–23.
- [5] Bidare, P., Bitharas, I., Ward, R., Attallah, M., and Moore, A., 2018, "Fluid and Particle Dynamics in Laser Powder Bed Fusion," *Acta Mater.*, **142**, pp. 107–120.
- [6] Ly, S., Rubenchik, A. M., Khairallah, S. A., Guss, G., and Matthews, M. J., 2017, "Metal Vapor Micro-jet Controls Material Redistribution in Laser Powder Bed Fusion Additive Manufacturing," *Sci. Rep.*, **7**(1), p. 4085.
- [7] Matthews, M. J., Guss, G., Khairallah, S. A., Rubenchik, A. M., Depond, P. J., and King, W. E., 2016, "Denudation of Metal Powder Layers in Laser Powder Bed Fusion Processes," *Acta Mater.*, **114**, pp. 33–42.
- [8] Guo, Q., Zhao, C., Escano, L. I., Young, Z., Xiong, L., Fezzaa, K., Everhart, W., Brown, B., Sun, T., and Chen, L., 2018, "Transient Dynamics of Powder Spattering in Laser Powder Bed Fusion Additive Manufacturing Process Revealed by in-Situ High-Speed High-Energy X-Ray Imaging," *Acta Mater.*, **151**, pp. 169–180.
- [9] Zhao, C., Fezzaa, K., Cunningham, R. W., Wen, H., De Carlo, F., Chen, L., Rollett, A. D., and Sun, T., 2017, "Real-time Monitoring of Laser Powder bed Fusion Process Using High-Speed X-ray Imaging and Diffraction," *Sci. Rep.*, **7**(1), p. 3602.
- [10] Cunningham, R., Zhao, C., Parab, N., Kantzos, C., Pauza, J., Fezzaa, K., Sun, T., and Rollett, A. D., 2019, "Keyhole Threshold and Morphology in Laser Melting Revealed by Ultrahigh-Speed X-Ray Imaging," *Science*, **363**(6429), pp. 849–852.
- [11] Gong, H., Rafi, K., Gu, H., Starr, T., and Stucker, B., 2014, "Analysis of Defect Generation in Ti-6Al-4V Parts Made Using Powder bed Fusion Additive Manufacturing Processes," *Addit. Manuf.*, **1**, pp. 87–98.
- [12] Snyder, J. C., and Thole, K. A., 2020, "Understanding Laser Powder Bed Fusion Surface Roughness," *ASME J. Manuf. Sci. Eng.*, **142**(7), p. 071003.
- [13] Nassar, A. R., Gundermann, M. A., Reutzel, E. W., Guerrier, P., Krane, M. H., and Weldon, M. J., 2019, "Formation Processes for Large Ejecta and Interactions With Melt Pool Formation in Powder Bed Fusion Additive Manufacturing," *Sci. Rep.*, **9**(1), p. 5038.
- [14] Moser, D., Yuksel, A., Cullinan, M., and Murthy, J., 2018, "Use of Detailed Particle Melt Modeling to Calculate Effective Melt Properties for Powders," *ASME J. Heat Transfer*, **140**(5), p. 052301.
- [15] Khairallah, S. A., Anderson, A. T., Rubenchik, A., and King, W. E., 2016, "Laser Powder-bed Fusion Additive Manufacturing: Physics of Complex Melt Flow and Formation Mechanisms of Pores, Spatter, and Denudation Zones," *Acta Mater.*, **108**, pp. 36–45.
- [16] Shrestha, S., and Kevin Chou, Y., 2019, "A Numerical Study on the Keyhole Formation During Laser Powder Bed Fusion Process," *ASME J. Manuf. Sci. Eng.*, **141**(10), p. 101002.
- [17] Körner, C., Attar, E., and Heinl, P., 2011, "Mesoscopic Simulation of Selective Beam Melting Processes," *J. Mater. Process. Technol.*, **211**(6), pp. 978–987.
- [18] Bayat, M., Thanki, A., Mohanty, S., Witvrouw, A., Yang, S., Thorborg, J., Tiedje, N. S., and Hattel, J. H., 2019, "Keyhole-induced Porosities in Laser-Based Powder Bed Fusion (L-PBF) of Ti6Al4V: High-Fidelity Modelling and Experimental Validation," *Addit. Manuf.*, **30**, p. 100835.
- [19] Yan, W., Ge, W., Qian, Y., Lin, S., Zhou, B., Liu, W. K., Lin, F., and Wagner, G. J., 2017, "Multi-physics Modeling of Single/Multiple-Track Defect Mechanisms in Electron Beam Selective Melting," *Acta Mater.*, **134**, pp. 324–333.
- [20] Yan, W., Qian, Y., Ge, W., Lin, S., Liu, W. K., Lin, F., and Wagner, G. J., 2018, "Meso-scale Modeling of Multiple-Layer Fabrication Process in Selective Electron Beam Melting: Inter-Layer/Track Voids Formation," *Mater. Des.*, **141**, pp. 210–219.
- [21] Masmoudi, A., Bolot, R., and Coddet, C., 2015, "Investigation of the Laser-Powder-Atmosphere Interaction Zone During the Selective Laser Melting Process," *J. Mater. Process. Technol.*, **225**, pp. 122–132.
- [22] Mayi, Y. A., Dal, M., Peyre, P., Bellet, M., Metton, C., Moriconi, C., and Fabbro, R., 2019, "Laser-induced Plume Investigated by Finite Element Modelling and Scaling of Particle Entrainment in Laser Powder Bed Fusion," *J. Phys. D: Appl. Phys.*, **53**(7), p. 075306.
- [23] Li, D., and Merkle, C. L., 2006, "A Unified Framework for Incompressible and Compressible Fluid Flows," *J. Hydrodyn. Ser. B*, **18**(3), pp. 113–119.
- [24] Glowinski, R., Pan, T.-W., Hesla, T. I., Joseph, D. D., and Periaux, J., 2001, "A Fictitious Domain Approach to the Direct Numerical Simulation of Incompressible Viscous Flow Past Moving Rigid Bodies: Application to Particulate Flow," *J. Comput. Phys.*, **169**(2), pp. 363–426.
- [25] Norouzi, H. R., Zarghami, R., Sotudeh-Gharebagh, R., and Mostoufi, N., 2016, *Coupled CFD-DEM Modeling: Formulation, Implementation and Application to Multiphase Flows*, John Wiley & Sons, Hoboken, NJ.
- [26] Grétarsson, J. T., Kwatra, N., and Fedkiw, R., 2011, "Numerically Stable Fluid-Structure Interactions Between Compressible Flow and Solid Structures," *J. Comput. Phys.*, **230**(8), pp. 3062–3084.
- [27] Uhlmann, M., 2005, "An Immersed Boundary Method With Direct Forcing for the Simulation of Particulate Flows," *J. Comput. Phys.*, **209**(2), pp. 448–476.
- [28] Anwar, A. B., and Pham, Q.-C., 2018, "Study of the Spatter Distribution on the Powder Bed During Selective Laser Melting," *Addit. Manuf.*, **22**, pp. 86–97.
- [29] Gunenthiram, V., Peyre, P., Schneider, M., Dal, M., Coste, F., Koutiri, I., and Fabbro, R., 2018, "Experimental Analysis of Spatter Generation and Melt-Pool Behavior During the Powder bed Laser Beam Melting Process," *J. Mater. Process. Technol.*, **251**, pp. 376–386.
- [30] Metals, A. S. M. A. S., 2004, *Titanium Ti-6Al-4V (Grade 5)*, ASM Material Data Sheet, ASM Aerospace Specification Metals Inc., FL.
- [31] Michels, A., Botzen, A., and Schuurman, W., 1954, "The Viscosity of Argon at Pressures up to 2000 Atmospheres," *Physica*, **20**(7–12), pp. 1141–1148.